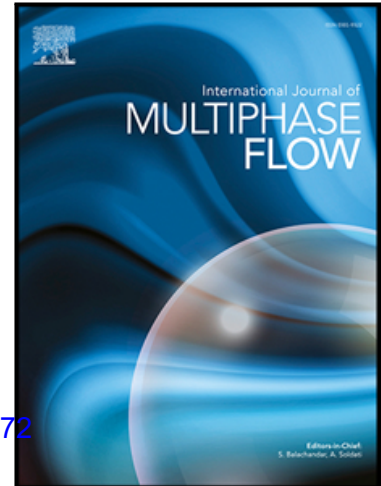# Journal Pre-proof

LES eulerian diffuse-interface modeling of fuel dense sprays near- and far-field

J.M. Desantes, J.M. García-Oliver, J.M. Pastor, I. Olmeda, A. Pandal, B. Naud

Please cite this article as: J.M. Desantes, J.M. García-Oliver, J.M. Pastor, I. Olmeda, A. Pandal, B. Naud, LES eulerian diffuse-interface modeling of fuel dense sprays near- and far-field, *International Journal of Multiphase Flow* (2020), doi: https://doi.org/10.1016/j.ijmultiphaseflow.2020.103272

Highlights

- Eulerian diffuse-interface spray model formulated into a LES turbulence framework

- Model assessment is performed for near and far-field using ECN Spray A database

- Near-nozzle projected fuel density distribution is properly captured

- Interfacial surface density LES formulation predicts spray atomization trends

- Global and local far-field spray metrics are accurately predicted

1

LES eulerian diffuse-interface modeling of fuel dense sprays near- and far-field

J.M. Desantes[a], J.M. García-Oliver[a], J.M. Pastor[a,*], I. Olmeda[a], A. Pandal[b], B. Naud[c]

[a]CMT-Motores Térmicos, Universitat Politècnica de València, Spain
[b]Área de Mecánica de Fluidos - Dpto. Energía, Universidad de Oviedo, Spain
[c]Modelling and Numerical Simulation Group, Energy Department, CIEMAT, Spain

Abstract

Engine fuel spray modeling still remains a challenge, especially in the dense near-nozzle region. This region is difficult to experimentally access and also to model due to the complex and rapid liquid and gas interaction. Modeling approaches based on Lagrangian particle tracking have failed in this area, while Eulerian modeling has proven to be particularly useful. Interface resolved methods are still limited to primary atomization academic configurations due to excessive computational requirements. To overcome those limitations, the single-fluid diffuse interface model known as Σ-Y, arises as a single-framework for spray simulations. Under the assumption of scale separation at high Reynolds and Weber numbers, liquid dispersion is modeled as turbulent mixing of a variable density flow. The concept of surface area density is used for representing liquid structures, regardless of the complexity of the interface.

In this work, a LES based implementation of the Σ-Y model in the Open-

*Corresponding author
Email address: jopasen@mot.upv.es (J.M. Pastor)

FOAM CFD library is applied to simulate the ECN Spray A configuration. Model assessment is performed for both near- and far-field spray development regions using different experimental diagnostics available from ECN database. The CFD model is able to capture near-nozzle fuel mass distribution and, after Σ equation constant calibration, interfacial surface area. Accurate predictions of spray far-field evolution in terms of liquid and vapor tip penetration and local velocity can be simultaneously achieved. Model accuracy is lower when compared to mixture fraction axial evolution, despite radial distribution profiles are well captured.

Keywords: Large Eddy Simulation, Eulerian, Diesel spray, Atomization, Engine Combustion Network (ECN), OpenFOAM®

1. Introduction

Fuel injection and subsequent spray development are critical factors for fuel-air mixture preparation, combustion and pollutants formation in engines. Atomization of the liquid phase occurs at extremely small length scales and high speeds in current injection systems, which complicates both the investigation and modeling of spray flow, especially in the near-nozzle region. The lack of optical accessibility, except by means of special diagnostic techniques [29, 48], hinders the flow characterization and the development of predictive primary atomization models.

At the most detailed level, complex modeling techniques devoted to capturing the liquid-gas interface [22, 34, 58] have been successfully applied to simulate initial spray development, but the computational requirements can make those calculations impractical for spray applications in combustion sys-

tems due to high Reynolds and Weber numbers. The most common spray modeling approaches, based on the representation of the liquid phase using a Lagrangian framework [17], are not well suited to represent this dense region [5], while fully Eulerian approaches have recently shown their potential to simulate near-nozzle physics [68, 5]. Under these conditions, a separation of the large scale flow features from the atomization process occurring at smaller scales can be assumed, as initially proposed by [64, 65]. Then large scale liquid dispersion is modeled as the turbulent mixing of a variable density fluid. In terms of atomization, the surface density concept, which represents the interfacial area per unit of volume, is introduced. The end result is a diffuse-interface treatment in an Eulerian framework, where unresolved interface features are modeled instead of being tracked.

These diffuse-interface Eulerian spray models have two common elements: a model for the transport of liquid and a model for the evolution of the interfacial surface area. The density of interfacial area is typically denoted by Sigma (Σ) while the liquid fraction is denoted by Y. Hence, we refer to the strictly Eulerian model as a Σ-Y approach, in contrast to ELSA (Eulerian-Lagrangian Spray Atomization), which includes a transition to Lagrangian particle tracking [33].

The transport of the liquid employs mass-averaged convection along with turbulent mixing. This model is derived from basic Favre averaging or filtering [13]. Thus, the accuracy of the liquid fraction transport is largely dependent on the accuracy of the two-phase turbulent modeling. Despite the challenges of such modeling, there is at least an extensive theoretical basis to deal with the unclosed terms [13, 1]. However, the model for the

4

interfacial surface density evolution is somewhat more speculative, with several unclosed terms [14]. Different interface modeling formulations have been applied to sprays as researchers have explored competing ideas of how these terms should be treated [8, 18, 34, 65].

In the present paper, a LES formulation of the Σ-Y model, based on [8], has been implemented to upgrade previous RANS formulations [21, 43]. This approach is assessed for compression ignition (CI) engine injection conditions, corresponding to the Engine Combustion Network (ECN) [20] Spray A. The potential of Σ-Y together with a LES turbulence approach for improved accuracy predictions of spray fuel distribution in the near-nozzle region has been recently shown by the authors [16] and in [2], compared to previous RANS based simulations [15, 44, 68]. Further assessment for both near- and far-field liquid dispersion is performed in the present work.

Far-field analysis requires the consideration of the fuel phase change process when injected at high-temperature and pressure conditions. According to experimental results by Siebers at Sandia National Laboratory (SNL) [59, 60, 61], the vaporization of CI (Diesel) sprays has been described as 'mixing-controlled', that implies faster interfacial mass and energy transport than turbulent mixing. The theoretical analysis performed by Poursadegh et al.[51], based on droplet formation and vaporization time scales, also indicates that Spray A conditions lies in the range where interfacial transport is not the limiting time scale. Different experimental and numerical studies have recently discussed about the sub- or super-critical regime of those fuel injection conditions [12, 10, 38]. According to [11], Spray A nominal condition still remain in the sub-critical regime, but high temperature and pressures

5

71 results in very small surface tension forces and extremely high Weber num-

72 ber. Under these conditions, the gas/liquid interface vanishes quickly and

73 phase-change may be evaluated from local thermal equilibrium assumptions

74 [21, 42, 38]. This approach has been followed in the present work in order to

75 simulate vaporizing sprays and to evaluate model performance downstream

76 the primary atomization region.

77 Experimental data for validation include near-nozzle x-ray based diag-

78 nostics conducted at Argonne National Laboratory (ANL) [29, 26] performed

79 at high-pressure but ambient temperature conditions. Considering primary

80 atomization, the interfacial density predictions have rarely been validated,

81 and these validations have been made in the context of downstream drop

82 size [7, 21]. A few prior examples used DNS simulations [34, 8] for model

83 evaluations, and in this paper the validation is performed via USAXS experi-

84 ments, which directly measures the interfacial surface density. As for far-field

85 validation, experimental characterization at high temperature from different

86 facilities [4] has been used. In particular, diagnostics include local velocity

87 [39] and mixture fraction [47] values measured by means of Particle Image Ve-

88 locimetry (PIV) and Rayleigh scattering, respectively. Spray tip penetration

89 has also been validated for both near- and far-field configurations.

90 After this introduction, the modeling approach and experimental results

91 used for validation are discussed. Next, the model setup is presented, fol-

92 lowed by the analysis of results, which has been divided into near-field spray

93 dispersion and surface density, and far field spray development. The paper

94 closes with the main conclusions.

6

2. Modeling approach

The Σ-Y model [65] proposes that, under large Reynolds and Weber numbers operating conditions, it is possible to assume a separation of the large scale flow features, such as liquid mass transport, from the atomization process occurring at smaller scales. The two-phase flow is then modeled as the turbulent mixing of a variable density fluid with a single velocity field, neglecting the effect of surface tension at large scales. This allows the direct simulation of the bulk fluid motion, while unresolved turbulent transport is modeled using standard closures. In this work, the model is formulated in a LES framework with implicit filtering, where filter size is then equal to the grid spacing, for turbulence modeling . Subgrid LES closures are based on the eddy-viscosity hypothesis and calculated by means of the σ-model [41], using a fixed model constant C_σ=1.5.

An indicator function is used to track the dispersion of the liquid phase, taking a value of unity in the liquid phase and zero in the gas phase. The filtered liquid volume fraction is denoted $(\overline{Y})$ and the mass weighted averaged fraction is defined as $(\tilde{Y} = \frac{\overline{\rho Y}}{\bar{\rho}})$. Favre averaging the transport equation for the liquid mass fraction yields Eq. (1)

$$\frac{\partial \bar{\rho}\tilde{Y}}{\partial t} + \frac{\partial \bar{\rho}\tilde{u}_i\tilde{Y}}{\partial x_i} = -\frac{\partial R_{iY}}{\partial x_i} - S_{evap} \tag{1}$$

where the last term accounts for phase change, which will be later discussed. The unclosed turbulent diffusion term, $R_{iY} = \bar{\rho}(\widetilde{u_i Y} - \tilde{u}_i\tilde{Y})$, that appears due to Favre averaging, can be physically related to relative velocity between phases, as described in [65, 13]. This term is modeled using a standard turbulent gradient flux model, which was successfully applied for Diesel-like

7

118 spray compared to DNS results [14]:

$$R_{iY} = \overline{\rho}(\widetilde{u_i Y} - \tilde{u}_i \tilde{Y}) = -\frac{\mu_{sgs}}{Sc_t}\frac{\partial \tilde{Y}}{\partial x_i} \tag{2}$$

119 where μ_{sgs} is the sub-grid turbulent viscosity and Sc_t is the turbulent Schmidt

120 number. Further developments for turbulent liquid flux closure can be found

121 in [1].

122 Under the assumption that the two phases form an immiscible mixture,

123 the mass-averaged value of the indicator function is related to the density

124 by:

$$\frac{1}{\overline{\rho}} = \frac{\tilde{Y}}{\rho_l} + \frac{1-\tilde{Y}}{\rho_g} \tag{3}$$

125 An equation of state is then assigned to each phase. The mixture of

126 gas phases obeys an ideal gas law, while for the liquid phase, density is

127 calculated following the Hankinson-Brobst-Thomson (HBT) correlation [53]

128 that accounts for pressure and temperature effects.

129 In order to account for liquid spray phase change, both an additional

130 transport equation (4) for vapor fuel mass fraction (Y_v) and also a procedure

131 for calculating the sink/source term, S_{evap}, of eq. 1 have been added. The

132 sub-grid scale flux term $\overline{\rho}(\widetilde{u_i Y_v} - \tilde{u}_i \tilde{Y}_v)$ in this equation, is solved by means

133 of a gradient closure as in eq. 1.

$$\frac{\partial \overline{\rho}\tilde{Y}_v}{\partial t} + \frac{\partial \overline{\rho}\tilde{u}_i \tilde{Y}_v}{\partial x_i} = \frac{\partial}{\partial x_i}\left(\frac{\mu_{eff}}{Sc}\frac{\partial \tilde{Y}_v}{\partial x_i}\right) + S_{evap} \tag{4}$$

134 The phase change model is developed in the framework of the diffuse-

135 interface spray approach, following previous authors proposals [21, 45]. The

136 main underlying hypothesis is that local thermodynamic equilibrium is con-

137 sidered within each computational cell, assuming that interfacial transport

8

138 is not limiting fuel vaporization. The liquid-vapor coexistence region is then
139 considered under adiabatic saturation condition in order to calculate the
140 equilibrium vapor fuel mass fraction $Y_{v,sat}$. The sink/source term for fuel liq-
141 uid/vapor transport equations (S_{evap}) is calculated in terms of a rate needed
142 to achieve this $Y_{v,sat}$. This can be written as in eq. 5, where τ_{evap} is a relax-
143 ation time set equal to the computational time step, in order to drive the
144 fuel vapor mass fraction Y_v towards the equilibrium $Y_{v,sat}$ at each time step.

$$S_{evap} = \bar{\rho}\frac{Y_{v,sat} - \tilde{Y}_v}{\tau_{evap}} \tag{5}$$

145 The following transport equation for the bulk mixture enthalpy is solved:

$$\frac{\partial \bar{\rho}\tilde{h}}{\partial t} + \frac{\partial \bar{\rho}\tilde{u}_i\tilde{h}}{\partial x_i} - \frac{\partial}{\partial x_i}\left(\alpha_{eff}\frac{\partial \tilde{h}}{\partial x_i}\right) = \frac{\partial \bar{p}}{\partial t} + \tilde{u}_i\frac{\partial \bar{p}}{\partial x_i} + \tau_{ij}\frac{\partial \tilde{u}_j}{\partial x_i} \tag{6}$$

146 Here α_{eff} is the effective turbulent thermal diffusivity and $\tau_{ij}\frac{\partial u_j}{\partial x_i}$ the viscous
147 dissipation. And then mixture temperature is obtained from:

$$\tilde{h}(T) = \tilde{Y} \cdot h_l(T) + (1 - \tilde{Y}) \cdot h_g(T) \tag{7}$$

148 where h_l and h_g denote the enthalpy of the liquid and gas phases respectively.
149 For the the liquid fuel, the Rowlinson-Bondi equation [53], based upon the
150 principle of corresponding states, is applied, while gas enthalpy is directly
151 obtained from the 7-coefficients NASA polynomials.

152 The solution of the previous equations fully characterizes the large-scale
153 bulk motion of the flow. As a result of the scales separation, atomization is
154 modeled by solving a transport equation for the evolution of the interfacial
155 surface area density Σ, which is defined as the liquid surface present per unit
156 volume at a given time and spatial position. This modeling approach has

9

157 started with the equation adopted by Vallet and Borghi [64], in which nearly

158 all the models in the literature are based. The transport equation for Σ reads

159 as shown in Eq. (8), assuming a first-order closure for the interface relative

160 velocity [34] and then obtained from a turbulent diffusive term, where D_Σ is

161 a suitable diffusion coefficient here taken as sub-grid turbulent viscosity μ_{sgs}

162 over turbulent Schmidt number Sc_t.

$$\frac{\partial \bar{\Sigma}}{\partial t} + \frac{\partial u_j \bar{\Sigma}}{\partial x_j} - \frac{\partial}{\partial x_j}\left(D_\Sigma \frac{\partial \bar{\Sigma}}{\partial x_j}\right) = \frac{\bar{\Sigma}}{\tau_\Sigma}\left(1 - \frac{\bar{\Sigma}}{\bar{\Sigma}_{eq}}\right) + S_{\Sigma_{evap}} + S_{\Sigma_{init}} \quad (8)$$

163 The first term at the RHS of this equation represents the surface gen-

164 eration and destruction, which is modelled in a restoration to equilibrium

165 form, where $\bar{\Sigma}_{eq}$ is an equilibrium or critical surface density and τ_Σ is the

166 associate time-scale. The surface energy is assumed locally at dynamic equi-

167 librium with the local kinetic energy in order to estimate this equilibrium

168 surface density. The $S_{\Sigma_{init}}$ term is a proper initialization source term, which

169 is necessary due to the fact that all the terms involved in the equation are

170 proportional to the interface surface density (Σ), and then ensures the com-

171 putation of interface due to the presence of the two phases. Finally, the

172 $S_{\Sigma_{evap}}$ term accounts for vaporization effects on interface surface [33].

173 Within this LES simulation framework, the surface density should be

174 postulated to describe the subgrid spray characteristics. Chesnel et al.[8]

175 discussed deeply about the different alternatives and concluded with a de-

176 scription where the presence of a minimum interface area is considered plus

177 the subgrid level surface density. Thus, the total evolution of the density of

178 interfacial surface area is given by:

10

$$\bar{\Sigma} = \bar{\Sigma}_{min} + \bar{\Sigma}' \tag{9}$$

179 where $\tilde{\Sigma}_{min}$ corresponds to the "minimal" surface density that can be found
180 for a given value of the resolved liquid volume fraction. It is inversely propor-
181 tional to the filter length scale (Δ_{LES}), which corresponds to grid spacing.
182 The constant α takes the value 2.4 [8].

$$\bar{\Sigma}_{min} = \frac{\alpha}{\Delta_{LES}} \sqrt{\overline{Y}(1 - \overline{Y})} \tag{10}$$

183 To close Eq.(9), a transport equation for the subgrid surface density is
184 defined in the following terms:

$$\frac{\partial \bar{\Sigma}'}{\partial t} + \frac{\partial \tilde{u}_j \bar{\Sigma}'}{\partial x_j} - \frac{\partial}{\partial x_j}\left(D_\Sigma \frac{\partial \bar{\Sigma}'}{\partial x_j} \right) - C_\Sigma \frac{\bar{\Sigma}}{\tau_t}\left(1 - \frac{\bar{\Sigma}}{\bar{\Sigma}_{eq}} \right) = 0 \tag{11}$$

185 where the coefficient C_Σ is used to relate the relaxation (τ_Σ) and subgrid
186 turbulent (τ_t) time scales:

$$\frac{1}{\tau_\Sigma} = \frac{C_\Sigma}{\tau_t} = C_\Sigma \frac{\epsilon_{sgs}}{k_{sgs}} \tag{12}$$

187 where k_{sgs} and ϵ_{sgs} are the subgrid turbulent kinetic energy and dissipation,
188 respectively. Finally, $\bar{\Sigma}_{eq}$, already mentioned, is the equilibrium or critical
189 surface density towards which the local surface density is driven. It is again
190 at least equal to the minimum surface density, and it can be described as a
191 function of the critical Weber number (We_{crit}) [18]:

$$\bar{\Sigma}_{eq} = \tilde{\Sigma}_{min} + \bar{\Sigma}'(We_{crit}) = \tilde{\Sigma}_{min} + 4 \frac{0.5(\rho_l + \rho_g)\overline{Y}(1 - \overline{Y})k_{sgs}}{\sigma \, We_{crit}} \tag{13}$$

11

192 This LES formulation does not require a initialization term such as in eq.

193 8 due the presence of a minimum surface density $\tilde{\Sigma}_{min}$ (see eq. 9 and eq. 11).

194 A term accounting for vaporization effect on $\tilde{\Sigma}'$ has not been yet developed,

195 and then has not been considered in this work. Note that the proposed term

196 for eq. 8 in [33] is valid for dispersed droplets but not for the dense zone

197 where, as it was pointed out by [34], is not clear if vaporization decreases or

198 increases the surface density. Nevertheless, the dependence of $\tilde{\Sigma}_{min}$ and $\bar{\Sigma}_{eq}$

199 on LVF includes vaporization effects in $\bar{\Sigma}$.

200 The previously described equations have been implemented into a finite

201 volume solver constructed by using the OpenFOAM [67] CFD library. This

202 implementation is based on the segregated pressure-based approach described

203 in [21, 63]. The pressure-equation for this multiphase compressible flow fol-

204 lows the proposal of [56] and [21]. Spatial discretization uses second-order

205 centered schemes, with convective fluxes solved by the Gamma [25] NVD

206 scheme. Time derivative terms are solved by a second-order backward scheme

207 and time step is defined by a maximum CFL of 0.4.

3. Experimental diagnostics

209 Experimental results available at the ECN [20] have been used to vali-

210 date the model results. For all cases, the single-hole Spray A nozzle,with a

211 nominal hole diameter of 90 μm, has been used. A detailed internal nozzle

212 geometric characterization [27], presented in Table 1, has been performed for

213 the injectors, where D, L and r denote nozzle orifice outlet diameter, length

214 and inlet radius, respectively. The nozzle convergence is described by the k-

215 factor, as defined in [36]. This smooth entrance and strong convergent angle

12

Table 1: Nozzle geometric characteristics for ECN Spray-A injectors

Injector Serial#	D[mm]	L/D[-]	r/D[-]	k-factor
210675	0.0894	11.5	0.23	2.7
210677	0.0837	12.3	0.18	3.2
210678	0.0886	11.8	0.21	2.8

₂₁₆ indicate that the nozzle is unlikely to cavitate, providing a simplification of

₂₁₇ the nozzle/spray connection.

₂₁₈   Different type of diagnostics have been used, which will be briefly pre-

₂₁₉ sented. The interested reader can find further information in the correspond-

₂₂₀ ing references [28, 26, 39, 47, 4]. Experimental conditions have been matched

₂₂₁ as closely as possible to the ECN Spray A specification [20], but injection

₂₂₂ is performed into an inert nitrogen atmosphere (Table 2). Near-nozzle ex-

₂₂₃ periments have been performed in an ambient temperature environment, i.e.

₂₂₄ non-vaporizing conditions, while far-field ones replicate Spray A ambient

₂₂₅ temperature, so that evaporation process occurs and the liquid phase disap-

₂₂₆ pears. In both cases, the same ambient density is used, which is expected to

₂₂₇ be a governing parameter in the fuel-air mixing process [40].

Table 2: Injection and ambient conditions for Spray A experiment

Fuel	n-Dodecane
Ambient composition	100% N2
Injection pressure [MPa]	150
Ambient temperature [K]	303/900
Ambient density [kg/m^3]	22.8
Fuel injection temperature [K]	343/363

₂₂₈   Those operating conditions results in the non-dimensional flow num-

13

229 bers presented in Table 3, showing that the spray operates under very high
230 Reynolds (Re) and Weber (We) numbers. The values for injection and am-
231 bient conditions variations performed for USAXS diagnostics presented in
232 section 3.1, are also included in this table.

Table 3: Non-dimensional flow numbers for experimental conditions

Case	Re_l	We_l	We_g	$\rho_l \ / \ \rho_g$
Spray A	4.94 x 10^4	1.03 x 10^6	3.28 x 10^4	31.2
P_{inj}=100 MPa	4.03 x 10^4	6.83 x 10^5	2.19 x 10^4	31.2
P_{inj}=50 MPa	2.85 x 10^4	3.42 x 10^5	1.09 x 10^4	31.2
ρ_{amb}=7.6 kg/m^3	4.94 x 10^4	1.03 x 10^6	1.09 x 10^4	93.7

233 *3.1. Near-nozzle diagnostics*

234   Near nozzle diagnostics include experiments carried out within the first
235 milimeters of spray development after injection. Liquid mass dispersion, sur-
236 face density and spray penetration are obtained by means X-Ray radiography,
237 Ultra-Small-Angle X-ray Scattering (USAXS) and schlieren visualization.

238 • X-ray radiography[28] experiments provide a path-length-integrated
239   measure of the fuel density along one beam path through the spray
240   due to the attenuation of beam radiation when travelling through the
241   spray. To measure the spatial distribution of the fuel, a two-dimensional
242   raster-scan approach is used, with each point measured from a different
243   set of spray events. To further improve the signal/noise ratio, each data
244   point is an average of 128-256 individual spray events. Time-resolved
245   data from those injections are used to measure the fuel distribution
246   with respect to time, as well as an average during the steady state.
247   Provided data represent the ensemble averaged three-dimensional fuel

14

density projected onto a plane. The fuel distribution data are thus reported as a Projected Mass Density (PMD), providing valuable information concerning liquid spray dispersion. Nozzle 210675 was used for these experiments.

- Ultra-Small-Angle X-ray Scattering (USAXS) is based on scattering effects[26], and enables the interrogation of the dense region of the spray providing quantitative information about the complex interface without resorting to the assumption that the liquid is in the form of droplets. The scattering intensity as a function of different vectors was measured at axial distances ranging from 1 to 20 mm downstream of the injection nozzle, at the centerline of the spray, from which the differential cross-section can be calculated, and related to the total shape and surface area per volume of fuel droplets, with post-processing performed using the Irena data analysis package[24]. As in X-ray radiography, nozzle 210675 was used in these measurements.

- In addition to the X-ray diagnostics, high-speed Schlieren visualization performed at SNL [20] has been used in order to characterize spray tip penetration. Nozzle 210677 was used for these experiments, and ambient temperature was 440 K, which can still be considered as a non-vaporizing environment.

3.2. Far-field diagnostics

Far field diagnostics consist of measurements spanning distances from the liquid length until the spray tip within an environment at 900 K. They include variables such as local velocity by means of Particle Image Velocimetry (PIV)

15

²⁷² and mixture fraction from Rayleigh Scattering Imaging, as well as global

²⁷³ metrics such as spray tip penetration and maximum liquid length.

²⁷⁴ • Local velocity fields for nozzle 210678 have been quantified at IF-

²⁷⁵ PEN constant volume vessel by means of Particle Image Velocimetry

²⁷⁶ (PIV)[39]. A high-speed Nd:YAG laser at 532 nm was used as a pulsed

²⁷⁷ laser source, which produced a light sheet intersecting the spray at the

²⁷⁸ symmetry axis. Images were acquired with a Photron SA1 camera.

²⁷⁹ 20 injection events were recorded, from which ensamble statistics are

²⁸⁰ reported.

²⁸¹ • Local mixture fraction has been measured for nozzle 210677 at Sandia

²⁸² constant volume vessel by means of Rayleigh Scattering [47]. In this

²⁸³ case, a low-speed Nd:YAG laser was used to form light sheet 40 mm

²⁸⁴ wide and 300 μm thick, also intersecting the spray at the symmetry

²⁸⁵ axis. The sheet spanned distances from the nozzle ranging from 17 to

²⁸⁶ 57 mm. On the collection side, an interference filter at the same wave-

²⁸⁷ length as the laser was coupled to the imaging system, a PIXIS1024B

²⁸⁸ camera.

²⁸⁹ • In terms of spray global metrics, high-speed imaging has been used

²⁹⁰ to resolve the spray tip penetration and maximum liquid length. The

²⁹¹ first one is measured by means of schlieren visualization for nozzle

²⁹² 210675 [4], while for the second one both Mie-Scattering (nozzle 210677)

²⁹³ and Diffuse Backlight Imaging (nozzle 210675) have been used [37, 46].

16

4. Model set-up

The computational domain comprises a cylindrical spray chamber with 20 mm in length ($\frac{x}{d} > 200$) and 10 mm in diameter ($\frac{r}{d} > 50$) for near-nozzle calculations. An extended domain of 80 mm x 30 mm has been used for including far-field spray development. There are 30 cells across nozzle outlet diameter (Inj. 210675, see Table 1), resulting in minimum grid spacing of ∼ 3 μm. The mesh is stretched in axial and radial directions, with maximum cell sizes of around 100 μm located in the outer edge of the domain, away from the spray zone. The grid consists of 6.7 and 12.6 million hexahedral cells for the near-nozzle and full-spray meshes, with the structure shown in Fig. 1. Grid convergence study has been performed using coarser and finer grid resolutions by modifying cell-to-cell expansion ratios, as indicated in Table 3. Concerning LES results quality assessment, previous work [16] showed that the resolved fraction of the turbulent kinetic energy was over 80 % within the spray region even for coarsest grid, which accomplishes the criteria proposed in [50].

Table 4: Characteristics of the different grid resolutions evaluated

Name	Axial expansion ratio	Radial expansion ratio	Number of cells
Grid 1	1.01	1.05	2.6e6
Grid 2	1.005	1.025	6.7e6
Grid 3	1.003	1.015	11.3e6

Injector flow has not directly included in the LES calculations, which requests an extremely high resolution grid to properly resolve the wall-bounded nozzle flow [2]. This would also require the additional complexity of modeling transient injector needle dynamics for accurate mass-flow rate predictions
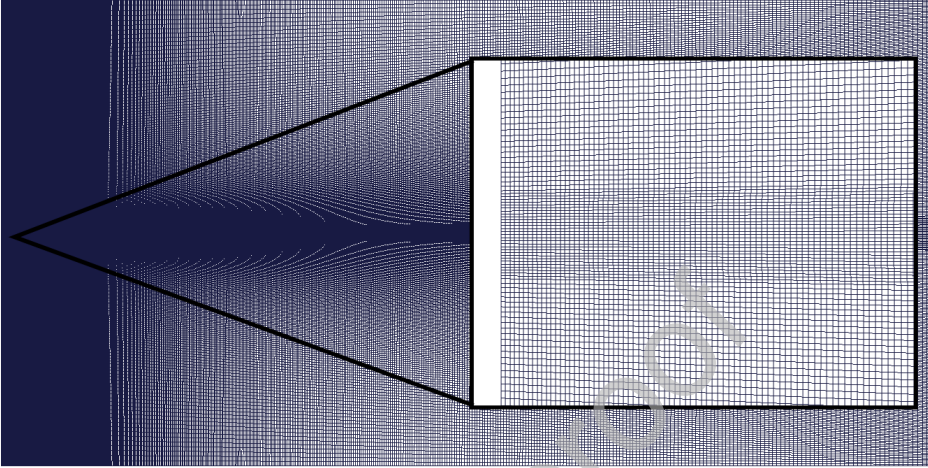
17

Figure 1: Computational domain slice showing grid structure. The insert shows a zoom around the nozzle outlet.

³¹⁴ [3, 6], and then the calculation domain would be limited to the initial spray

³¹⁵ region for manageable computational costs. Injection conditions are then ap-

³¹⁶ plied at nozzle outlet by means of an inlet boundary condition (BC) where the

³¹⁷ time-dependent mass-flow rate [27] obtained from CMT virtual injection rate

³¹⁸ generator [9], is used in order to get the bulk injection velocity. A synthetic

³¹⁹ turbulent generator [16], based on the proposals by [31, 30] and following

³²⁰ the method described in [55], has been used in order to generate correlated

³²¹ turbulent fluctuations over the mean outlet profile. This profile follows a

³²² $1/7^{th}$ power-law and the turbulent intensity (I) was obtained from previous

³²³ nozzle flow modeling results [44]. As pointed out in [16], this value ranges

³²⁴ between 3 and 5 % depending on the turbulence model. A non-slip condition

³²⁵ is applied in the surface around the nozzle outlet, while non-reflective BCs

18

326 are applied on the other domain surfaces, in order to avoid wave reflection on
327 those open ends. The so-called *waveTransmissive* BC has been used, which is
328 an approximation of the NSCBC [49] that can be applied to the semi-implicit
329 algorithms in OpenFOAM.

5. Results and Discussion

5.1. Near-field spray dispersion

332 Projected Mass Density (PMD) data has been used in order to evaluate
333 liquid spray dispersion calculations in the near-nozzle region. Line-of-sight
334 integration has been applied to predicted fuel density in order to replicate
335 x-ray radiography measurements. Simulation results are averaged between
336 0.4 and 1.2 ms after the Start-of-Injection (SoI), such as in experimental
337 data [19]. In Fig. 2 measured and predicted PMD contours are presented,
338 showing that the simulations capture the spray fuel distribution in the near-
339 nozzle region.

340 A more detailed comparison can be performed from PMD profiles at dif-
341 ferent axial positions shown in Fig. 3. Experimental data has been centered
342 about the FWHM in order to correct asymmetries due to offset hole on the
343 nozzle tip and spray axis tilt [48]. It is shown that the model is able to ac-
344 curately predict PMD profiles shortly after the nozzle outlet, at x=0.1 mm
345 ($\frac{x}{d} \approx 1$), and also from dense spray region (x=2 mm) to more dispersed axial
346 positions (x=6 mm). Concerning grid convergence of CFD results, the finest
347 grids are seen to yield nearly the same results, while the coarser one shows
348 higher peak and narrower profiles when moving to downstream locations.
349 Then the intermediate grid resolution has been used in further calculations.

19

(a) x-ray data

(b) LES I=3% Grid 2 data
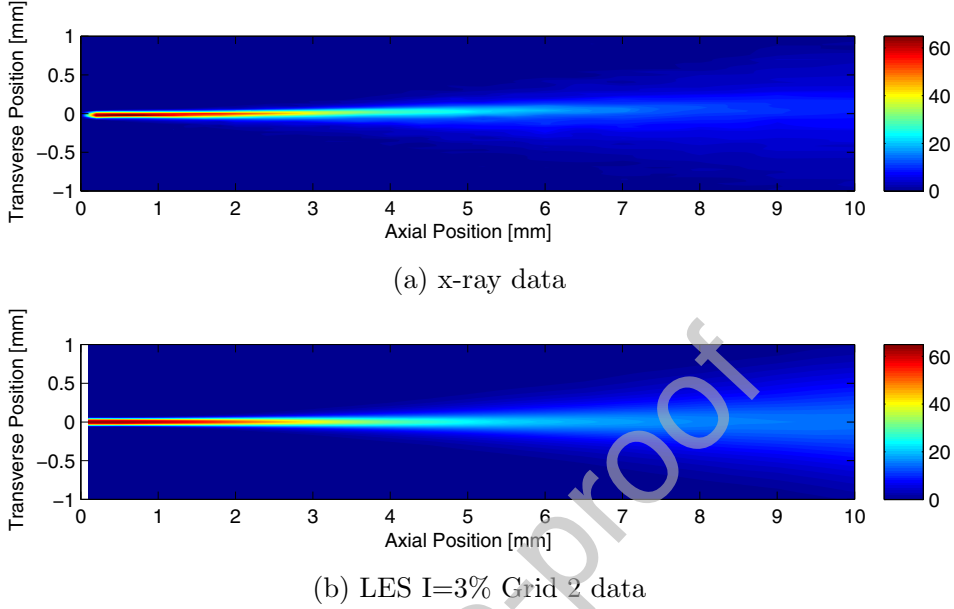
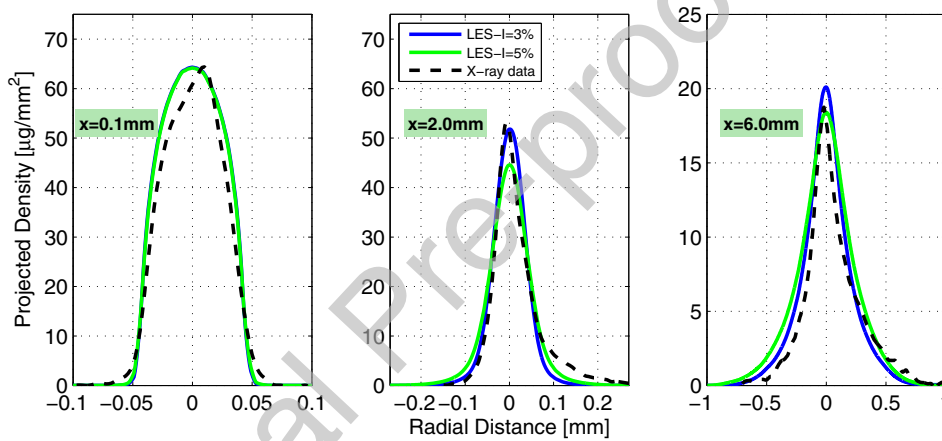Figure 2: Projected mass density $[\mu g/mm^2]$ distributions

Figure 3: Computed (I=3%) and measured [28] profiles of PMD at axial locations of 0.1 mm, 2 mm, and 6 mm downstream of the nozzle exit
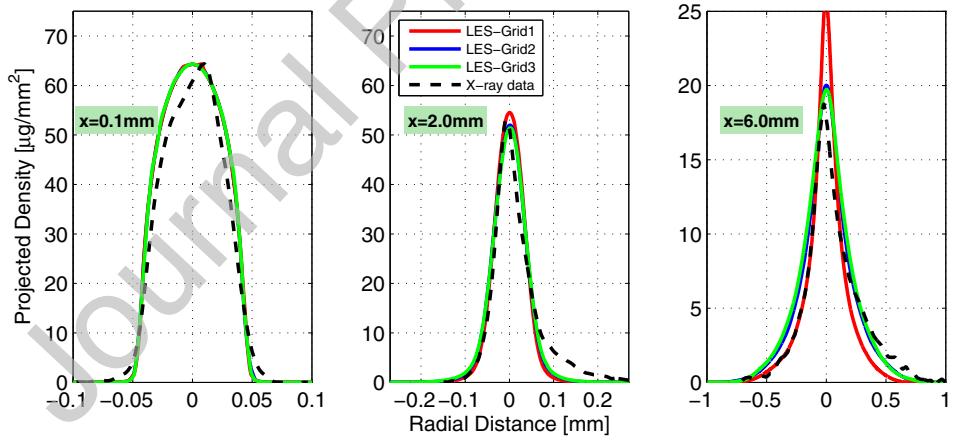
350   As indicate in Sec. 4, nozzle flow is not included in the calculations, but
351 PMD predictions obtained here are as accurate as recently shown in [2]. They

20

³⁵² used a similar approach but solving injector flow, which may indicate that
³⁵³ the inlet boundary setup properly reproduces nozzle outlet flow conditions,
³⁵⁴ taking benefit from the simplified geometry of the single-hole tapered high
³⁵⁵ $\frac{L}{D}$ ratio Spray A nozzle. It is then interesting to evaluate the impact of
³⁵⁶ inlet boundary conditions shown Fig. 4: higher turbulence intensities values
³⁵⁷ (I=5%), as used in [32], widens fuel PMD distribution and decrease peak
³⁵⁸ value, showing how initial perturbations affect near-nozzle spray mixing.

Figure 4: Computed and measured [28] profiles of PMD at axial locations of 0.1 mm, 2 mm, and 6 mm downstream of the nozzle exit

³⁵⁹ Further insight on spray structure can be obtained from the tomographic
³⁶⁰ reconstruction of the PMD data made by Pickett et al. [48], providing liquid
³⁶¹ volume fraction (LVF) results. In Fig. 5, the axial profile of the reconstructed
³⁶² LVF is compared with CFD computed profiles, indicating that the model is
³⁶³ able to capture the intact core and the LVF profile decay along the spray axis.
³⁶⁴ This result also confirms the model ability to predict fuel spray dispersion
³⁶⁵ from the dense near nozzle to sparse regions downstream. It is also depicted
³⁶⁶ that increasing nozzle outlet turbulent fluctuation from 3 to 5% results in

367 shorter intact core and lower on-axis LVF in the dense spray region.
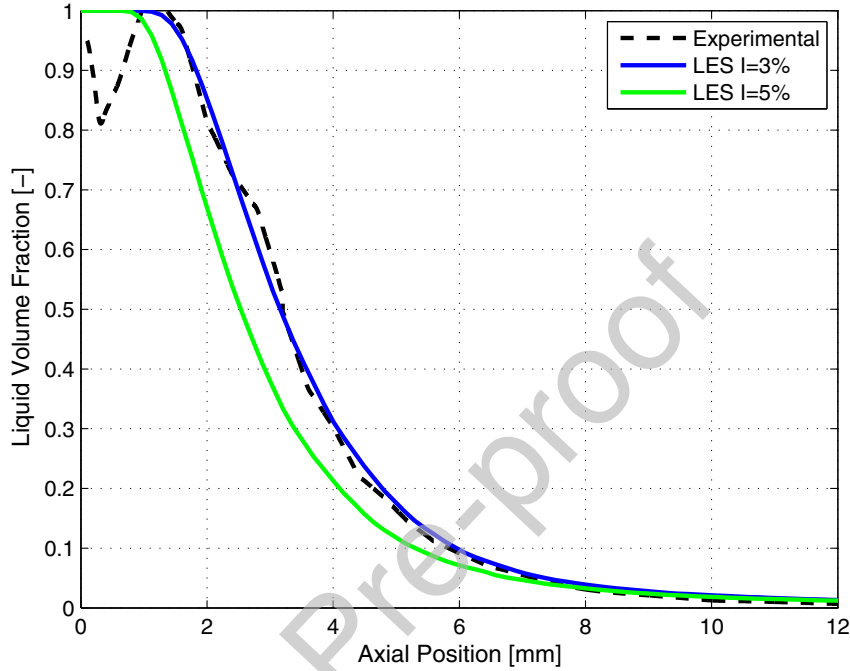
Figure 5: Computed and measured [48] centerline Liquid Volume Fraction

368 5.2. Spray atomization: surface density

369 Following the liquid spray dispersion results previously assessed, this sec-
370 tion deals with the evaluation of interfacial surface area predictions compared
371 to USAXS results used for spray atomization characterization.

372 As indicated in Sec.2, the equilibrium surface density ($\bar{\Sigma}_{eq}$) defined by a
373 critical Weber number (We_c), and a relaxation time-scale towards this $\bar{\Sigma}_{eq}$,
374 are required to compute interfacial surface density Σ. Those parameters are
375 yet not fully established, though recent numerical studies based in two-phase
376 DNS results [14, 18] have provided initial insight. In this work, experimental

22
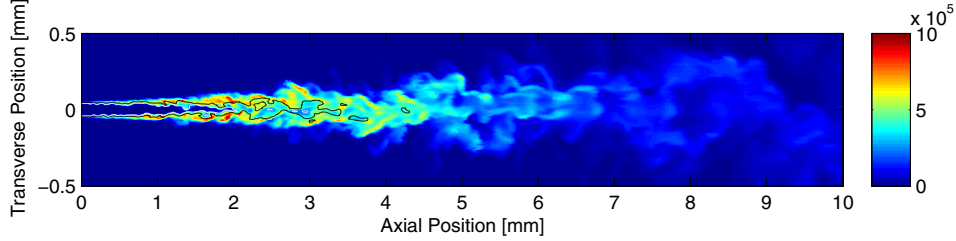
Figure 6: Contours of surface area density $(\bar{\Sigma})$ $[\mathrm{m}^{-1}]$ at 1 ms aSOI

377 USAXS data [43] have been used to evaluate and select those parameters for
378 further calculations.
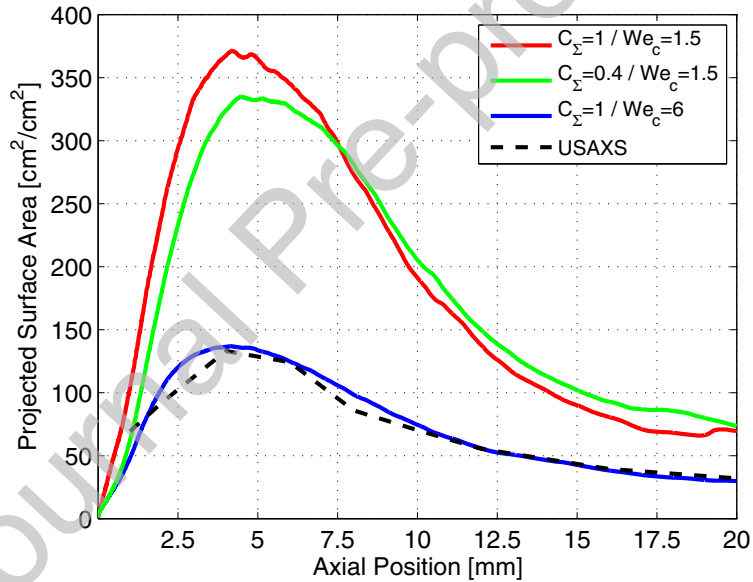
Figure 7: Computed and measured [43] projected surface area on spray axis.

379 An example of model predictions of Σ at reference condition is presented
380 in Fig. 6. It can be observed that interface production starts after the spray
381 core (defined by LVF=0.9 white iso-line) and peaks downstream, around
382 LVF=0.5 regions indicated by the black iso-line in the figure.

23

383 In order to compare with available USAXS data, computational results
384 are time-averaged and projected on the spray axis, which results in path-
385 integrated data presented in Fig. 7. This figure shows the effect of We_c
386 and C_Σ on the predictions. The proposed $We_c = 1.5$ by [14] results in an
387 over-predicted projected surface area, even with slower relaxation time-scales
388 using $C_\Sigma = 0.4$, as suggested in [18]. Fair agreement was found with $We_c=6$,
389 which lies in the range proposed by [8].
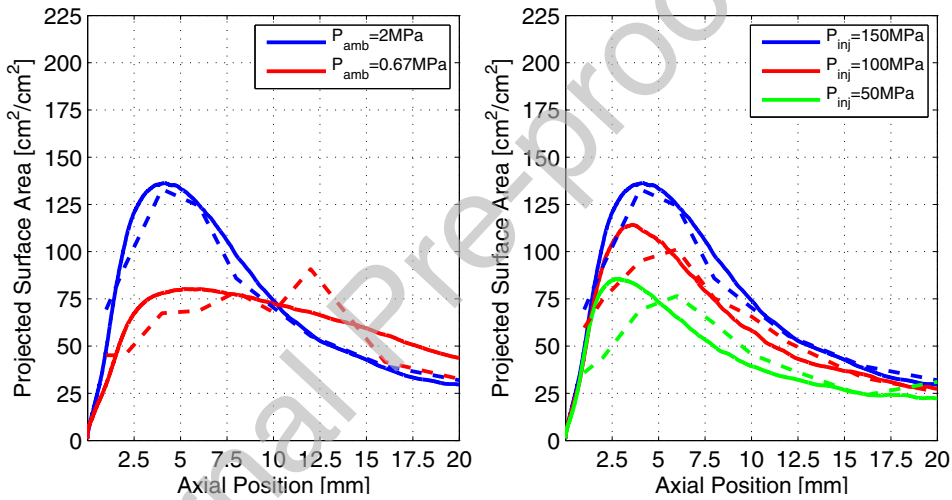
Figure 8: Computed (solid lines) and measured (dotted lines)[43] projected surface area on spray axis. Ambient density (left) and injection pressure (right) variations.

390 Additional simulations with those constant values for Σ calculation have
391 been performed. Fig. 8 shows that lower ambient density results in a slower
392 interfacial surface growth close to the nozzle, due to slower atomization,
393 which is properly captured by the CFD model. Injection pressure effect is
394 also well predicted by the simulations, i.e. lower injection pressure results in
395 reduced interfacial density (see Fig. 8). In this case the model over-predicts
396 peak projected Σ for reduced injection pressures, despite downstream axial

24

decay is accurately captured. In general, LES predictions improve previous authors results with this modeling approach under a RANS framework [16, 43].

5.3. Far-field spray development: non-vaporizing spray

An important feature of the present modeling approach is the fact that it enables accurate predictions for both near- and far-field spray zones. In the previous section, the analysis has been performed on liquid fuel dispersion and atomization, which happen in the near-field. The present section will show results in the far-field. The analysis starts with the liquid spray tip penetration under non-vaporizing conditions, which actually links both zones. For this purpose Fig. 9 compares modeling and measured results from two independent experimental datasets, namely that from x-ray radiography, which provides detailed information of spray evolution in the initial stages, and schlieren imaging from SNL, which also includes the whole spray evolution, but at the expense of lower spatial and temporal resolutions. Results indicate that the model is able to predict this metric. Extensive studies in the literature (e.g.[40]) have evidenced that Diesel spray tip penetration under both non-vaporizing and vaporizing conditions is governed by momentum exchange between the injected fuel and the ambient gas. In simplified terms, the spray can be considered as a constant momentum flux flow, which entrains air due to the increase in radial width. By simple momentum flux considerations, this exchange between fuel and air results in a decreasing velocity flow, as shown by spray tip evolution. Remarkable accuracy is achieved by the model both during the initial stages as well as later on, when the flow is fully-developed.
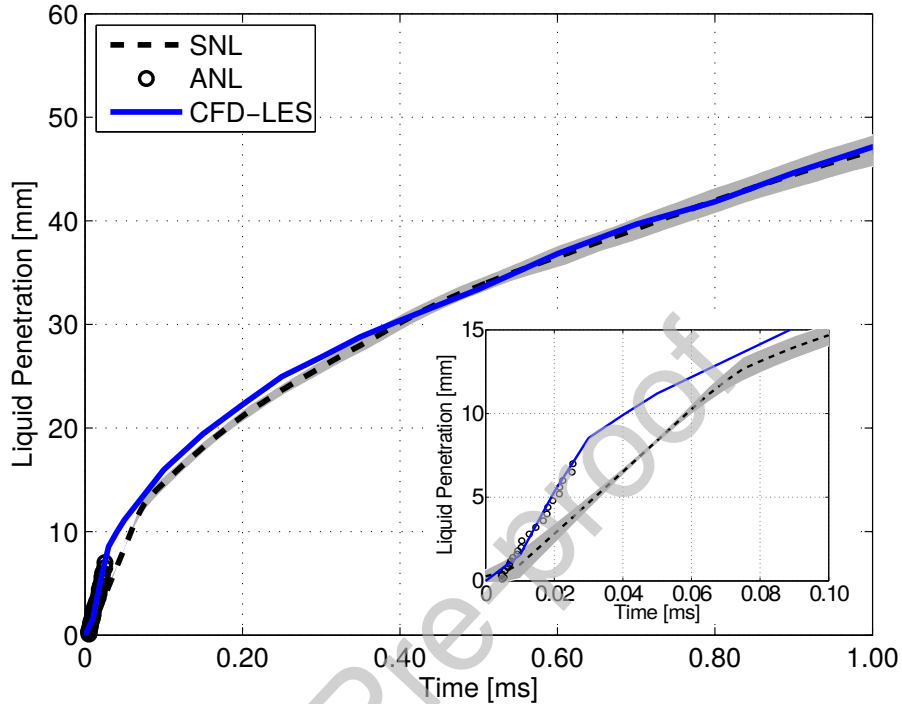
25

Figure 9: Computed and measured spray tip penetration. The shaded area represents the 95 % confidence interval in measurements. Two datasets are included, the initial penetration from X-ray (Inj. 210675 at T_a=303 K), and the later one from schlieren visualization (Inj. 210677 at T_a=440 K).

422   Starting with the penetration, Diesel-like fuel sprays injected under engine
423   conditions are known to behave very similarly to a gas jet. This feature has
424   been explored to assess the results of the LES calculations in Fig. 10 and 11.
425   First, radial profiles of the normalized mean axial component of the velocity
426   vector (U) are shown at different distances to the nozzle, which evidence a
427   self-similar behaviour, as found in gas jets [23, 62]. This results in a linear
428   increase of the inverse of the axial velocity with the distance to the nozzle, as
429   Fig. 10 shows. A similar behaviour is observed for the fluctuating component
430   of the axial velocity (u'), with self-similar radial distribution, as well as a

26

431 constant value on the axis with increasing distance to the nozzle (Fig. 11).
432 It must be noted that detailed studies on isodense gas jets, show this self-
433 similarity starting from a distance to the nozzle in the order of 15 and 25
434 nozzle diameters for the first and second moments [57], respectively . Liquid
435 fuel sprays, however, evolve in a flow with a high density drop. The first
436 consequence is that self-similarity starts from a larger distance to the nozzle,
437 if expressed in terms of nozzle diameters. A more suitable scaling factor is the
438 equivalent diameter $D_{eq} = D\sqrt{\frac{\rho_l}{\rho_g}}$, introduced by Ricou and Spalding [54],
439 which is a more appropriate scaling in cases where fuel-to-ambient density
440 ratio is different from unity. Fig. 10 shows that the self-similar behaviour
441 starts at around 30 D_{eq}, when local to ambient gas density ratio $\left(\frac{\rho}{\rho_g}\right)$ on the
442 axis levels off.
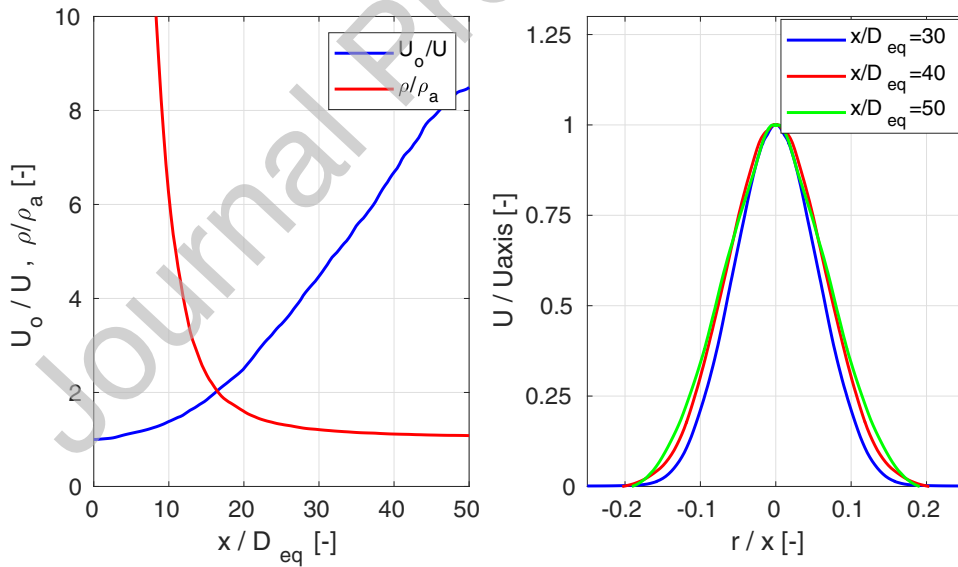
Figure 10: Computed mean normalized axial velocity on the spray axis (left) and at radial cross-sections (right). Left figure also includes the local to ambient density ratio.
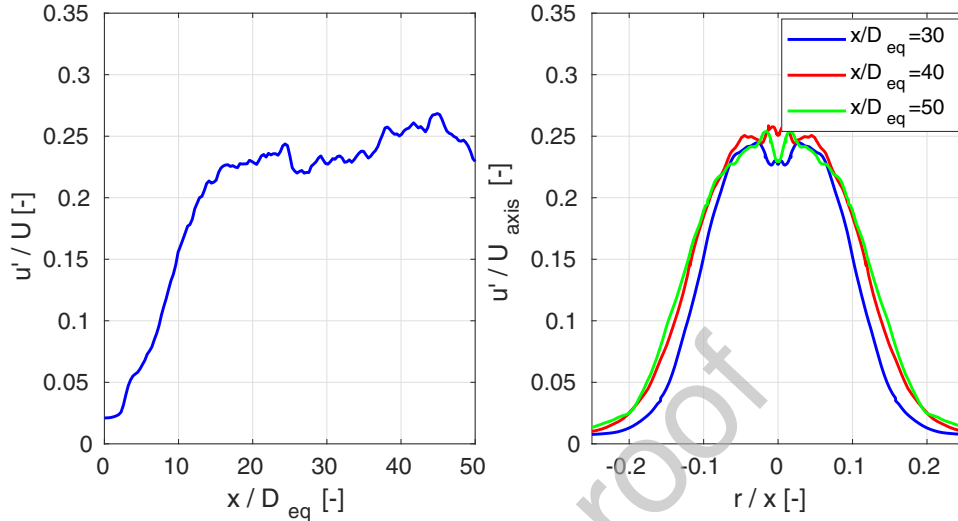
27

Figure 11: Computed r.m.s fluctuations of axial velocity on the spray axis (left) and at radial cross-sections (right).

5.4. Far-field spray development: vaporizing spray

In addition to the non-vaporizing results presented so far, the model has also been applied for nominal high-temperature ECN Spray A, which corresponds to typical CI engine conditions, and multiple experimental diagnostics are available.

Fig. 12 shows simulated vapor and liquid spray penetration, defined according ECN standards [20]. The model fairly agrees with experimental spray evolution for Schlieren imaging [4]. The liquid spray penetration is also well captured by the model, which lies between the experimental data acquired by means of Mie-scattering [4] and DBI [37] techniques. Note that the liquid-length fluctuations are caused by the detached structures in the liquid spray tip shown in Fig. 15. The accuracy of vapor and liquid predictions is similar to that of [38], but the current approach is also able to accurately describe

28

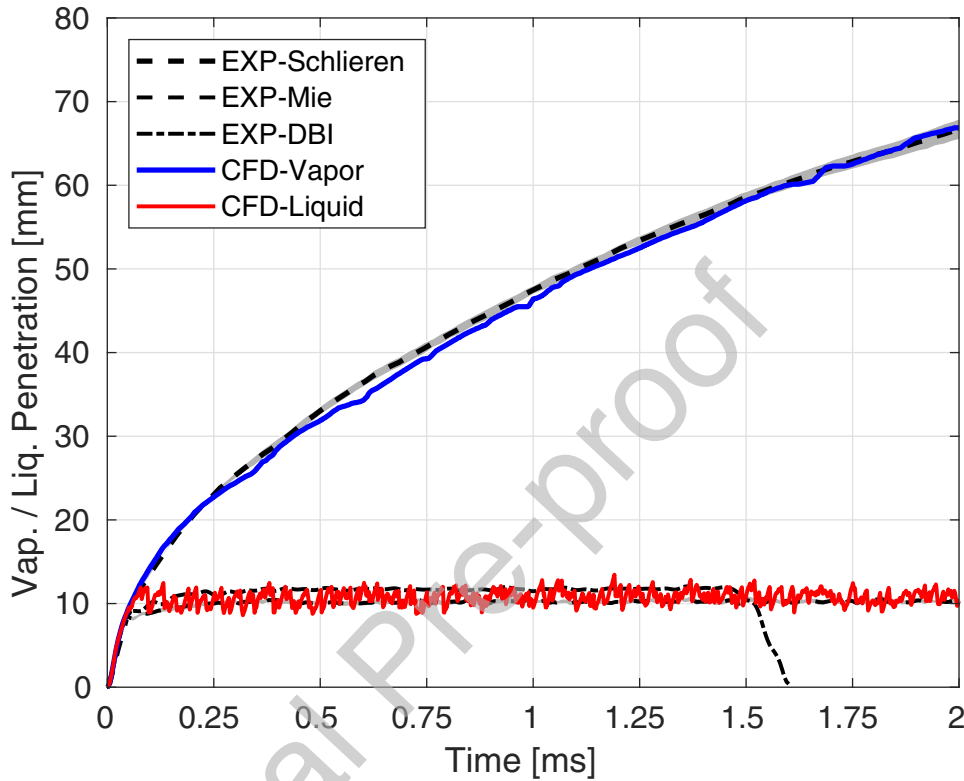456 the near-nozzle flow, as previously stated.

Figure 12: Computed and measured [4] vapor and liquid spray tip penetration. Inj. 210675 and 210677 at nominal Spray A condition T_a=900 K. The shaded area represents the 95 % confidence interval in measurements

457 This result is backed up by the analysis of local velocity shown in Fig. 13,
458 where both the axial and radial distribution of axial velocity are compared.
459 Experimental data for comparison [39] are available at 1.5 ms, along the
460 quasi-steady part of the spray. Modelling results have been time-averaged
461 from 1 to 2 ms and radial profiles correspond to azimuthal-averaged data.
462 Accuracy on the axis is remarkable, and radial results have been normalized
463 by those on the axis, showing that the radial width of the flow is also properly

29

predicted, as well as the self-similar features of the axial velocity distribution.

Finally, the model evaluation closes with the comparison of mixture frac-tion distribution, which corresponds to fuel vapor mass fraction downstream the liquid spray, in Fig. 14, with a similar layout as in the local velocity case. Averaging of CFD results is performed within the same time window. In this case, the model is seen clearly to underestimate this parameter on the axis, indicating a trend to overmix. In spite of that, radial flow width is properly captured.
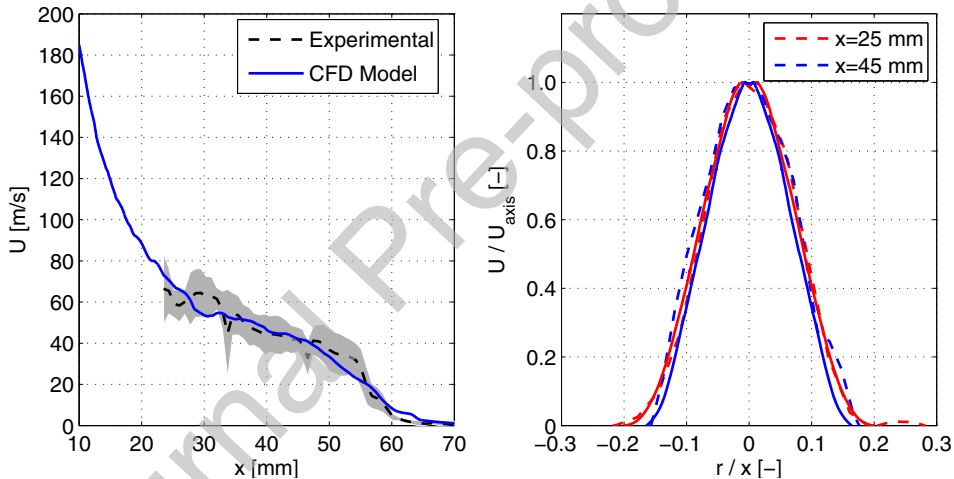
Figure 13: Computed and measured [39] mean axial component of the velocity on the spray axis (left) and at radial cross-sections at x=25 and 45 mm (right). Inj. 210678 at nominal Spray A condition T_a=900 K. The shaded area represents the 95 % confidence interval in measurements.

Until this point, the model has been extensively validated against dif-ferent experiments, described in section 3, under both non-vaporizing and vaporizing conditions. Note that those diagnostics have provided a detailed description of near-filed spray structure under high-pressure but ambient temperature environment [28, 26], and downstream the liquid spray for va-

30
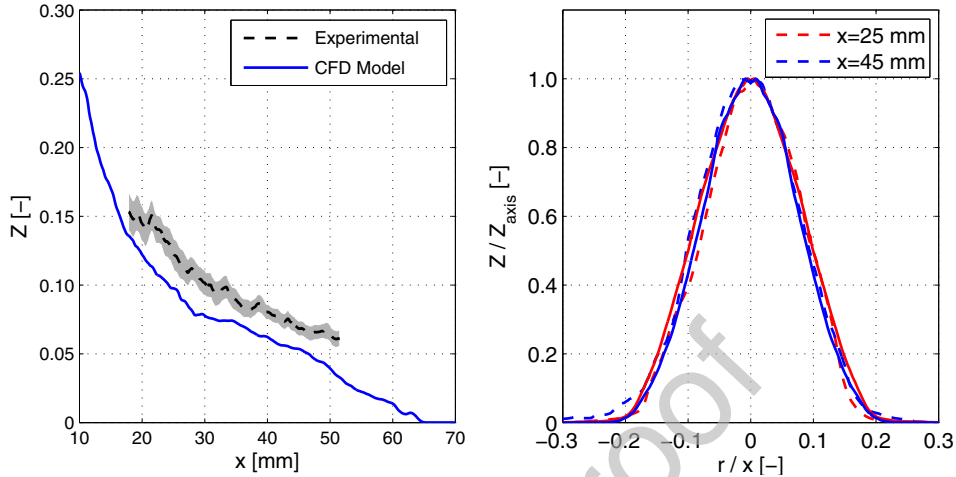
Figure 14: Computed and measured [47] mean mixture fraction (fuel vapor mass fraction) on the spray axis (left) and at radial cross-sections at x=25 and 45 mm (right). Inj. 210677 at nominal Spray A condition T_a=900 K. The shaded area represents the 95 % confidence interval in measurements.

porizing conditions [39, 47]. Further discussion is provided here on model results that can provide additional insight into the behaviour of the liquid spray under high temperature conditions.

The predicted spray structure is shown at Fig. 15, where the contours of vapor fuel mass fraction and a isosurface of LVF=1.5 x 10^{-3} defining the liquid spray phase limit as suggested in [38], are plotted. Vapor fuel concentration peaks around the liquid spray limit with values close to the saturated vapor-liquid equilibrium fuel mass fraction [45] evaluated from adiabatic mixing and the ambient and fuel boundary conditions.

Fig.16a presents the predicted liquid volume fraction (LVF) contours, where LVF is found to be larger than 0.1 over 50% of the liquid spray length (in the order of 10 mm). This indicates that vaporization takes place within the dense spray region, confirming that local flow is far from being dispersed
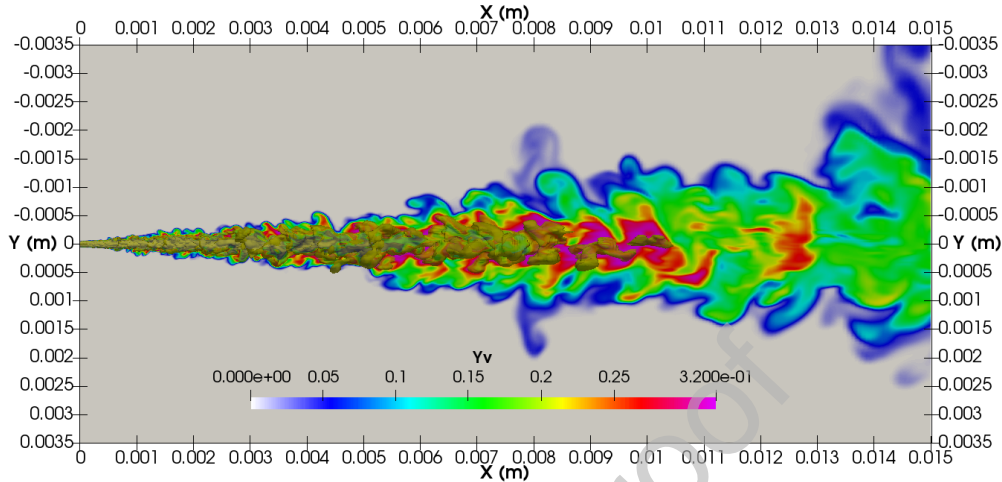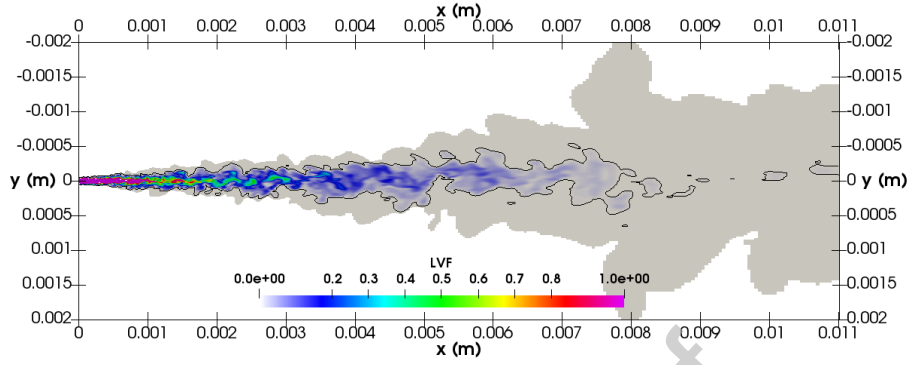
31

Figure 15: Computed vapor mass fraction (Y_v) on a symmetry plane and LVF=1.5 x 10^{-3} isosurface at nominal Spray A condition T_a=900 K.

⁴⁹⁰ in terms of droplets. The model also provides the characteristic size of liquid
⁴⁹¹ structures in terms of Sauter Mean Diameter (SMD) from Σ and Y pre-
⁴⁹² dictions ($SMD = \frac{6\bar{Y}}{\bar{\Sigma}}$), an example of which is shown in Fig.16b. The SMD
⁴⁹³ abruptly decreases shortly downstream the liquid intact core, in agreement to
⁴⁹⁴ experimental results combining PMD and USAXS diagnostics [26] performed
⁴⁹⁵ under non-vaporizing conditions. Further downstream, SMD remains almost
⁴⁹⁶ stable, with drop sizes around 1-2 x 10^{-6} m in the dense spray regions, also
⁴⁹⁷ similar to [26] results, and eventually decreases due to vaporization effects as
⁴⁹⁸ liquid fuel approaches the liquid spray limits.
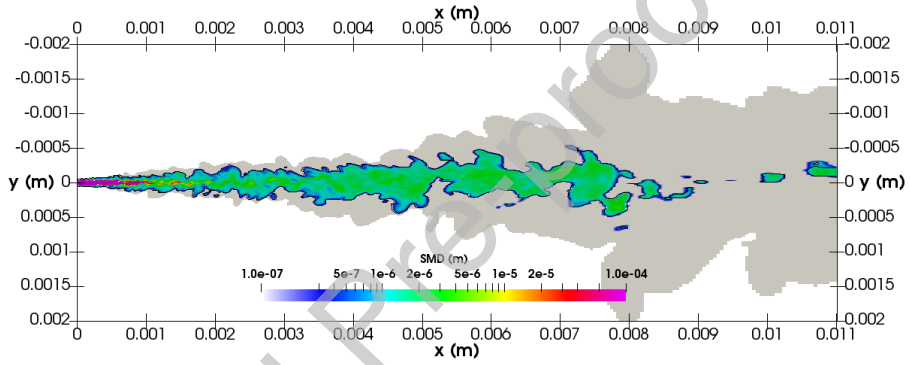
⁴⁹⁹ The characteristic time scales can be obtained from simulation flow con-
⁵⁰⁰ ditions in order to evaluate the vaporization modeling approach assumptions.
⁵⁰¹ The droplet vaporization time scale, computed as an isolated droplet in a con-
⁵⁰² vective environment as [51], from those drop sizes and the relative velocity
⁵⁰³ based on single velocity field fluctuations [52], is $\approx$ 5 x 10^{-7}s. If we esti-

32

504 mate the liquid spray mixing time scale from local velocity and vaporization

505 length, it turn out to be ≈ 2 x 10^{-5}s, which is also higher than vaporization

506 ones. Even subgrid turbulent time scales are bigger, as shown in Fig.16c,

507 which indicate values in the order of 2 x 10^{-6} s within the liquid spray.

(a) Liquid Volume Fraction (LVF) contours
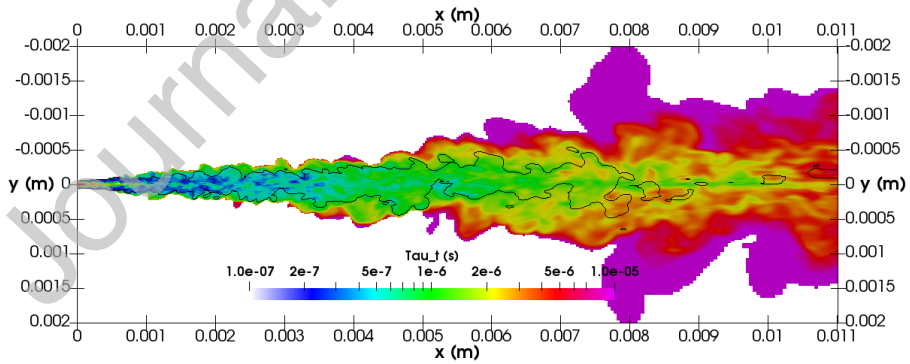

(b) Sauter Mead Diameter (SMD) contours

(c) Subgrid turbulent time-scale (τ_t) contours

Figure 16: Computed results on a symmetry plane at nominal Spray A condition T_a=900 K. The shaded contour represents vapor fuel spray defined by Y_v=1 x $10^{-3}$and the black isoline (LVF=1.5 x 10^{-3}) defines the liquid spray.

34

508 Summarizing, model results confirm that most of the liquid mass evolves
509 in a high-density region, which is governed by air entrainment. A relatively
510 constant droplet size is obtained from the end of the intact core up to the
511 maximum liquid length, where droplets disappear due to evaporation. The
512 fact that for this type of sprays such processes occur relatively close to the
513 nozzle suggests that particle methods based on dispersed flow assumptions
514 may be not valid for these conditions, and supports the current Eulerian
515 approach based on dynamic and thermal equilibrium.

6. Summary and Conclusions

517 This work presents a LES implementation of the diffuse-interface Σ-Y
518 spray model applied for high-pressure fuel injection. The model performance
519 has been assessed for complete spray development simulations corresponding
520 to the ECN Spray-A condition.

521 Near-nozzle spray model validation has been performed by comparing
522 with x-ray radiography data in terms of projected mass density and liquid-
523 volume fraction. Spray flow has been modeled by using a synthetic turbulence
524 boundary condition at the nozzle exit, which replaces expensive nozzle-flow
525 calculations. Fuel dispersion is properly predicted, with accuracy level similar
526 to recent results that include nozzle internal geometry. Nevertheless, it is
527 shown that turbulent fluctuations have a noticeable impact in near-nozzle
528 spray dispersion. Detailed internal flow calculations are then required for a
529 fully predictive calculation of spray development when using more complex
530 nozzle geometries.

531 Concerning spray atomization, a LES specific formulation has been used
532 for interfacial surface density modeling. Predictions have been directly com-

pared to measurements obtained using USAXS technique. The equilibrium surface density, defined by a critical We number, has been calibrated in a single operation point. Without further adjustment the model was able to predict both injection pressure and ambient density variations, improving previous results. This outcome shows the potential of the LES Σ equation for predicting complex atomization features in those high We and Re dense spray region. It also enables the use of this information for including more complex liquid/gas interaction in fuel dispersion Y-equation.

Besides near-nozzle predictions, far-field spray development has also been evaluated. Global metrics such as spray tip penetration and maximum liquid length are accurately predicted, both under non-vaporizing and vaporizing conditions. Local analysis shows that velocity field predictions also match experimental measurements, so local flow dynamics is well-captured. However, mixture fraction tends to be underpredicted, in spite of the fact that the width of the radial distribution is adequately captured. Similar conclusions can be drawn from other LES calculations of Spray A test case [69, 66], only few approaches [38, 35] are able to capture the mixing field. Nevertheless, none of these cases evaluates at the same time the near-nozzle atomization and spray dispersion together with the far-field spray evolution.

Model results confirm that under ECN Spray A conditions liquid vaporizes within a high density region, where droplet diffusion timescales are much lower than turbulent mixing timescales. These results hint at the limitations in disperse droplet methods, and confirms the advantages of the present modelling approach to capture the evolution of such high dense multiphase flows.

36

In summary, the present contribution shows that the proposed LES diffuse-interface Eulerian framework can capture both near-nozzle atomization and dispersion features, together with far-field local flow and mixing, with no need for an exhaustive calibration of model constants. This is a highly relevant result for detailed spray calculations with a single framework.

Acknowledgements

Authors also thank the shared X-ray radiography and Ultra-Small-Angle X-ray Scattering measurements performed at Argonne National Laboratory by the following authors: Daniel J. Duke, Jan Ilavsky, Katarzyna E. Matusik, Brandon A. Sforzo, Alan L. Kastengren, and Christopher F. Powell.

References

[1] Andreini, A., Bianchini, C., Puggelli, S., and Demoulin, F. X., Development of a turbulent liquid flux model for Eulerian-Eulerian multiphase flow simulations, *International Journal of Multiphase Flow*, vol. **81**, pp. 88–103, 2016.
URL http://dx.doi.org/10.1016/j.ijmultiphaseflow.2016.02.003

[2] Anez, J., Ahmed, A., Hecht, N., Duret, B., Reveillon, J., and Demoulin, F., Eulerian-Lagrangian Spray Atomization model coupled with Interface Capturing Method for Diesel injectors, *International Journal of Multiphase Flow*, vol. **113**, pp. 325–342, 2019.
URL https://www.sciencedirect.com/science/article/pii/S0301932218303550

37

[3] Baldwin, E. T., Grover, R. O., Parrish, S. E., Duke, D. J., Matusik, K. E., Powell, C. F., Kastengren, A. L., and Schmidt, D. P., String flash-boiling in gasoline direct injection simulations with transient needle motion, *International Journal of Multiphase Flow*, vol. **87**, pp. 90–101, 2016.
URL http://dx.doi.org/10.1016/j.ijmultiphaseflow.2016.09.004

[4] Bardi, M., Payri, R., Malbec, L., Brunneaux, G., Pickett, L., Manin, J., Bazyn, T., and Genzale, C., Engine combustion network: Comparison of spray development,vaporization and combustion in different combustion vessels, *Atomization and Sprays*, vol. **22**, pp. 807–842, 2012.

[5] Battistoni, M., Magnotti, G. M., Genzale, C. L., Arienti, M., Matusik, K. E., Duke, D. J., Giraldo, J., Ilavsky, J., Kastengren, A. L., Powell, C. F., and Marti-Aldaravi, P., Experimental and Computational Investigation of Sub-critical Near-Nozzle Spray Structure and Primary Atomization in the Engine Combustion Network Spray D, *SAE Technical Paper*, no. 2018-01-0277, pp. 1–15, 2018.

[6] Battistoni, M., Som, S., and Powell, C. F., Highly resolved Eulerian simulations of fuel spray transients in single and multi-hole injectors: Nozzle flow and near-exit dynamics, *Fuel*, vol. **251**, pp. 709–729, 2019.
URL https://www.sciencedirect.com/science/article/pii/S0016236119306313

[7] Beheshti, N., Burluka, A., and Fairweather, M., Assessment of $\Sigma - Y$ liq model predictions for air-assisted atomisation, *Theoretical and Computational Fluid Dynamics*, vol. **21**, no. 5, pp. 381–397, 2007.

[8] Chesnel, J., Reveillon, J., Ménard, T., and Demoulin, F. X., Large eddy simulation of liquid jet atomization, *Atomization and Sprays*, vol. **21**, no. 9, pp. 711–736, 2011.

[9] CMT, Virtual injection rate generator, 2018.
URL http://www.cmt.upv.es

[10] Crua, C., Heikal, M. R., and Gold, M. R., Microscopic imaging of the initial stage of diesel spray formation, *Fuel*, vol. **157**, pp. 140–150, 2015.
URL http://dx.doi.org/10.1016/j.fuel.2015.04.041

[11] Crua, C., Manin, J., and Pickett, L. M., On the transcritical mixing of fuels at diesel engine conditions, *Fuel*, vol. **208**, pp. 535–548, 2017.
URL http://dx.doi.org/10.1016/j.fuel.2017.06.091

[12] Dahms, R. N., Manin, J., Pickett, L. M., and Oefelein, J. C., Understanding high-pressure gas-liquid interface phenomena in diesel engines, *Proceedings of the Combustion Institute*, vol. **34**, no. 1, pp. 1667 – 1675, 2013.

[13] Demoulin, F., Beau, P., Blokkeel, G., Mura, A., and Borghi, R., A new model for turbulent flows with large density fluctuations: application to liquid atomization, *Atomization and Sprays*, vol. **17**, pp. 315–345, 2007.

[14] Demoulin, F.-X., Reveillon, J., Duret, B., Bouali, Z., Desjonqueres, P., and Menard, T., Toward using direct numerical simulation to improve primary break-up modeling, *Atomization and Sprays*, vol. **23**, no. 11, pp. 957–980, 2013.

[15] Desantes, J., García-Oliver, J., Pastor, J., Pandal, A., Baldwin, E., and Schmidt, D., Coupled / decoupled spray simulation comparison of the ECN spray a condition with the $\Sigma - Y$ eulerian atomization model, *International Journal of Multiphase Flow*, vol. **80**, pp. 89 – 99, 2016.

[16] Desantes, J. M., García-Oliver, J. M., Pastor, J. M., Pandal, A., Naud, B., Matusik, K., Duke, D., Kastengren, A., Powell, C., and Schmidt, D. P., Modelling and validation of near-field Diesel spray CFD simulations based on the Σ-Y model, *ILASS2017 - 28th European Conference on Liquid Atomization and Spray Systems, September 6-8, Valencia, Spain*, 2017.
URL http://dx.doi.org/10.4995/ILASS2017.2017.4715

[17] Dukowicz, J., A particle fluid numerical model for liquid sprays, *Journal of Computational Physics*, vol. **35**, no. 2, pp. 229–253, 1980.

[18] Duret, B., Reveillon, J., Menard, T., and Demoulin, F., Improving primary atomization modeling through dns of two-phase flows, *International Journal of Multiphase Flow*, vol. **55**, pp. 130 – 137, 2013.
URL http://www.sciencedirect.com/science/article/pii/S0301932213000773

[19] ECN, LVF data archive, 2014.
URL http://www.sandia.gov/ecn/argonne/assets/datafiles/mixture/rad675.php

[20] ECN, Engine combustion network data archive, 2018.
URL http://www.sandia.gov/ecn/

[21] García-Oliver, J., Pastor, J., Pandal, A., Trask, N., Baldwin, E., and Schmidt, D., Diesel spray CFD simulations based on the $\Sigma - Y$ eulerian atomization model, *Atomization and Sprays*, vol. **23**, pp. 71–95, 2013.

39

[22] Gorokhovski, M. and Herrmann, M., Modeling primary atomization, *Annual Review of Fluid Mechanics*, vol. **40**, pp. 343–366, 2008.

[23] Hussein, H. J., Capp, S. P., and George, W. K., Velocity measurements in a high-reynolds-number, momentum-conserving, axisymmetric, turbulent jet, *Journal of Fluid Mechanics*, vol. **258**, p. 31–75, 1994.

[24] Ilavsky, J. and Jemian, P. R., *Irena*: tool suite for modeling and analysis of small-angle scattering, *Journal of Applied Crystallography*, vol. **42**, no. 2, pp. 347–353, 2009.

[25] Jasak, H., Weller, H. G., and Gosman, A. D., High resolution NVD differencing scheme for arbitrarily unstructured meshes, *International Journal for Numerical Methods in Fluids*, vol. **31**, no. 2, pp. 431–449, 1999.

[26] Kastengren, A., Ilavsky, J., Viera, J. P., Payri, R., Duke, D. J., Swantek, A., Tilocco, F. Z., Sovis, N., and Powell, C. F., Measurements of droplet size in shear-driven atomization using ultra-small angle x-ray scattering, *International Journal of Multiphase Flow*, vol. **92**, pp. 131–139, 2017.

[27] Kastengren, A., Tilocco, F. Z., Powell, C. F., Manin, J., Pickett, L. M., Payri, R., and Bazyn, T., Engine combustion network (ECN):measurements of nozzle geometry and hydraulic behavior, *Atomization and Sprays*, vol. **22**, pp. 1011–1052, 2012.

[28] Kastengren, A. L., , Tilocco, F. Z., Duke, D. J., Powell, C. F., Seoksu, M., and Xusheng, Z., Time-resolved x-ray radiography of diesel injectors from the engine combustion network, *ICLASS Paper*, no. 1369, 2012.

[29] Kastengren, A. L., Powell, C. F., Wang, Y., Im, K.-S., and Wang, J., X-ray radiography measurements of diesel spray structure at engine-like ambient density, *Atomization and Sprays*, vol. **19**, no. 11, pp. 1031–1044, 2009.

[30] Klein, M., Sadiki, A., and Janicka, J., A digital filter based generation of inflow data for spatially developing direct numerical or large eddy simulations, *Journal of Computational Physics*, vol. **186**, no. 2, pp. 652–665, 2003.

[31] Kraichnan, R. H., Diffusion by a Random Velocity Field, *Physics of Fluids*, vol. **13**, no. 1, pp. 22 – 30, 1970.
URL https://aip.scitation.org/doi/10.1063/1.1692799

[32] Lacaze, G., Misdariis, A., Ruiz, A., and Oefelein, J. C., Analysis of high-pressure diesel fuel injection processes using les with real-fluid thermo-dynamics and transport, *Proceedings of the Combustion Institute*, vol. **35**, no. 2, pp. 1603 – 1611, 2015.
URL http://www.sciencedirect.com/science/article/pii/S1540748914002302

[33] Lebas, R., Beau, P.-a., Blokkeel, G., and Demoulin, F.-X., ELSA Model for Atomization: To Benefit of the Eulerian and Lagrangian Descriptions of the Liquid Phase, *Proceedings of the 10th International Conference on Liquid Atomization and Spray Systems, ICLASS 2006, Aug.27-Sept.1, Kyoto, Japan*, pp. 565–572, 2006.

[34] Lebas, R., Menard, T., Beau, P., Berlemont, A., and Demoulin, F., Numerical simulation of primary break-up and atomization: DNS and modeling study, *International Journal of Multiphase Flow*, vol. **35**, pp. 247–260, 2009.

[35] Ma, P. C., Wu, H., Jaravel, T., Bravo, L., and Ihme, M., Large-eddy simulations of transcritical injection and auto-ignition using diffuse-interface method and finite-rate chemistry, *Proceedings of the Combustion Institute*, vol. **37**, no. 3, pp. 3303–3310, 2018.
URL https://www.sciencedirect.com/science/article/pii/S1540748918300646

[36] Macián, V., Bermúdez, V., Payri, R., and Gimeno, J., New technique for determination of internal geometry of a diesel nozzles with the use of silicone methodology, *Experimental Techniques*, vol. **37**, pp. 39–43, 2003.

[37] Manin, J., Bardi, M., and Pickett, L. M., Evaluation of the liquid length via diffused back-illumination imaging in vaporizing diesel sprays, *The Proceedings of the International symposium on diagnostics and modeling of combustion in internal combustion engines COMODIA*, vol. **2012.8**, pp. 665–673, 2012.

[38] Matheis, J. and Hickel, S., Multi-component vapor-liquid equilibrium model for LES of high-pressure fuel injection and application to ECN Spray A, *International Journal of Multiphase Flow*, vol. **99**, pp. 294–311, 2018.
URL http://www.sciencedirect.com/science/article/pii/S0301932217301076

[39] Meijer, M., Malbec, L., Brunneaux, G., and Somers, L., Engine combustion network : 'spray a' basic measurements and advanced diagnostics, *Proceedings of the 12th International Conference on Liquid Atomization and Spray Systems, ICLASS 2012, 2-6 September, Heidelberg, Germany*, 2012.

[40] Naber, J. and Siebers, D., Effects of gas density and vaporization on penetration and dispersion of diesel sprays, *SAE Technical Paper*, no. 960034, 1996.

[41] Nicoud, F., Toda, H. B., Cabrit, O., Bose, S., and Lee, J., Using singular values to build a subgrid-scale model for large eddy simulations, *Physics of Fluids*, no. 8, 2011.

[42] Oefelein, J., Dahms, R., and Lacaze, G., Detailed modeling and simulation of high-pressure fuel injection processes in diesel engines, *SAE Int. J. Engines*, vol. **5**, no. 3, pp. 1410 – 1419, 2012.

[43] Pandal, A., Pastor, J. M., Payri, R., Kastengren, A., Duke, D., Matusik, K., Giraldo, J. S., Powell, C., and Schmidt, D., Computational and experimental investigation of interfacial area in near-field diesel spray simulation, *SAE Int. J. Fuels Lubr.*, vol. **10**, pp. 423 – 431, 2017.

[44] Pandal, A., Payri, R., García-Oliver, J., and Pastor, J., Optimization of spray break-up cfd simulations by combining σ-y eulerian atomization model with a response surface methodology under diesel engine-like conditions (ECN Spray A), *Computers and Fluids*, vol. **156**, pp. 9 – 20, 2017.

[45] Pastor, J., García-Oliver, J., Pastor, J., and Vera-Tudela, W., One-dimensional diesel spray modeling of multicomponent fuels, *Atomization and Sprays*, vol. **25**, no. 6, pp. 485–517, 2015.

[46] Pickett, L., Genzale, C., Manin, J., Malbec, L., and Hermant, L., Measurement uncertainty of liquid penetration in evaporating diesel sprays, *ILASS-Americas 2011, Ventura, California, May 15-18, Paper No. 2011-111*, 2011.

[47] Pickett, L., Manin, J., Genzale, C., Siebers, D., Musculus, M., and Idicheria, C., Relationship between diesel fues spray vapor penetration/dispersion and local fuel mixture fraction, *SAE Int. J. Engines*, vol. **4**, pp. 764–799, 2011.

[48] Pickett, L., Manin, J., Kastengren, A., and Powell, C., Comparison of near-field structure and growth of a diesel spray using light-based optical microscopy and x-ray radiography, *SAE Int. J. Engines*, vol. **7**, no. 2, 2014.

[49] Poinsot, T. and Lelef, S., Boundary conditions for direct simulations of compressible viscous flows, *Journal of Computational Physics*, vol. **101**, no. 1, pp. 104 – 129, 1992.
URL http://www.sciencedirect.com/science/article/pii/0021999192900462

[50] Pope, S. B., Ten questions concerning the large-eddy simulation of turbulent flows, *New Journal of Physics*, vol. **6**, 2004.

[51] Poursadegh, F., Lacey, J. S., Brear, M. J., and Gordon, R. L., On the Fuel Spray Transition to Dense Fluid Mixing at Reciprocating Engine Conditions, *Energy and Fuels*, vol. **31**, no. 6, pp. 6445–6454, 2017.

[52] Puggelli, S., Palanti, L., Andreini, A., and Demoulin, F.-X., Development of an evaporation model for the dense spray region in Eulerian-Eulerian multiphase flow simulations, *ILASS2017 - 28th European Conference on Liquid Atomization and Spray Systems, September 6-8, Valencia, Spain*, 2017.

[53] Reid, R., Prausnitz, J., and Poling, B., *The Properties of Gases and Liquids*, McGraw-Hill, 1987.

[54] Ricou, F. P. and Spalding, D. B., Measurements of entrainment by axisymmetrical turbulent jets, *Journal of Fluid Mechanics*, vol. **11**, no. 1, p. 21–32, 1961.

[55] Robert, A., Martinez, L., Tillou, J., and Richard, S., Eulerian – Eulerian Large Eddy Simulations Applied to Non-Reactive Transient Diesel Sprays, *Oil & Gas Science and Technology – Revue d'IFP Energies nouvelles*, vol. **69**, no. 1, pp. 141–154, 2014.
URL http://ogst.ifenergiesnouvelles.fr/10.2516/ogst/2013140

[56] Schmidt, D., Gopalakrishnan, S., and Jasak, H., Multi-dimensional simulation of thermal non-equilibrium channel flow, *International Journal of Multiphase Flow*, vol. **36**, no. 4, pp. 284 – 292, 2010.
URL http://www.sciencedirect.com/science/article/pii/S030193220900192X

[57] Shin, D. H., Sandberg, R. D., and Richardson, E. S., Self-similarity of fluid residence time statistics in a turbulent round jet, *Journal of Fluid Mechanics*, vol. **823**, pp. 1–25, 2017.

[58] Shinjo, J. and Umemura, A., Simulation of liquid jet primary breakup: Dynamics of ligament and droplet formation, *International Journal of Multiphase Flow*, vol. **36**, no. 7, pp. 513–532, 2010.

[59] Siebers, D., Liquid-phase fuel penetration in diesel sprays, *Trans. SAE*, vol. **107**, pp. 1205–1227, 1998.

[60] Siebers, D., Scaling liquid-phase fuel penetration in diesel sprays based on mixing-limited vaporization, *Trans. SAE*, vol. **108**, pp. 703–728, 1999.

[61] Siebers, D. L., 2008. Recent developments on diesel fuel jets under quiescent conditions, *Flow and combustion in reciprocating engines.* Arcoumanis, C. and Kamimoto, T. (Eds.). Springer-Verlag, Berlin, pp. 257–308.

[62] Taub, G. N., Lee, H., Balachandar, S., and Sherif, S. A., A direct numerical simulation study of higher order statistics in a turbulent round jet, *Physics of Fluids*, vol. **25**, no. 11, p. 115102, 2013.
URL http://aip.scitation.org/doi/10.1063/1.4829045

[63] Trask, N., Schmidt, D., Lightfoot, M., and Danczyk, S., Compressible modeling of the internal flow in a gas-centered swirl-coaxial fuel injector, *Journal of Propulsion and Power*, vol. **28(4)**, pp. 685–693, 2012.

[64] Vallet, A. and Borghi, R., Modélisation Eulerienne de l'atomisation d'un jet liquide, *C.R. Acad. Sci, Paris*, vol. **327**, pp. 1015–1020, 1999.

[65] Vallet, A., Burluka, A., and Borghi, R., Development of a Eulerian model for the "atomization" of a liquid jet, *Atomization and Sprays*, vol. **11**, pp. 619–642, 2001.

[66] Wehrfritz, A., Kaario, O., Vuorinen, V., and Somers, B., Large Eddy Simulation of n-dodecane spray flames using Flamelet Generated Manifolds, *Combustion and Flame*, vol. **167**, pp. 113–131, 2016.
URL https://www.sciencedirect.com/science/article/pii/S0010218016000754?via%3Dihub

[67] Weller, H., Tabor, G., Jasak, H., and Fureby, C., A tensorial approach to computational continuum mechanics using object-oriented techniques, *Computers in Physics*, vol. **12**, pp. 620–631, 1998.

[68] Xue, Q., Battistoni, M., Powell, C., Longman, D., Quan, S., Pomraning, E., Senecal, P., Schmidt, D., and Som, S., An eulerian CFD model and x-ray radiography for coupled nozzle flow and spray in internal combustion engines, *International Journal of Multiphase Flow*, vol. **70**, pp. 77 – 88, 2015.

[69] Xue, Q., Som, S., Senecal, P. K., and Pomraning, E., Large eddy simulation of fuel-spray under non-reacting ic engine conditions, *Atomization and Sprays*, vol. **23**, no. 10, pp. 925–955, 2013.

44

Declaration of interests

☒ The authors declare that they have no known competing financial interests or personal relationships that could have appeared to influence the work reported in this paper.

811

☐The authors declare the following financial interests/personal relationships which may be considered as potential competing interests: